

Single-atom cobalt on N-doped reduced graphene oxide pushes the oxygen reduction reaction toward 4-electron pathway

Original

Single-atom cobalt on N-doped reduced graphene oxide pushes the oxygen reduction reaction toward 4-electron pathway / Risplendi, Francesca; Garino, Nadia; Zeng, Juqin; Sacco, Adriano; Mehta, Shweta; Deriu, Chiara; Fabris, Laura; Fontana, Marco; Chiodoni, Angelica; Cicero, Giancarlo; Castellino, Micaela. - In: NPJ 2D MATERIALS AND APPLICATIONS. - ISSN 2397-7132. - 9:1(2025). [10.1038/s41699-025-00604-x]

Availability:

This version is available at: 11583/3003744 since: 2025-10-07T15:38:47Z

Publisher:

Springer Nature

Published

DOI:10.1038/s41699-025-00604-x

Terms of use:

This article is made available under terms and conditions as specified in the corresponding bibliographic description in the repository

Publisher copyright

(Article begins on next page)

<https://doi.org/10.1038/s41699-025-00604-x>

Single-atom cobalt on N-doped reduced graphene oxide pushes the oxygen reduction reaction toward 4-electron pathway

Check for updates

Francesca Risplendi¹ ✉, Nadia Garino^{1,2}, Juqin Zeng^{1,2}, Adriano Sacco², Shweta Mehta¹, Chiara Deriu¹, Laura Fabris¹, Marco Fontana^{1,2}, Angelica Chiodoni², Giancarlo Cicero¹ & Micaela Castellino^{1,2} ✉

We present a cobalt-based single-atom catalyst (SAC) anchored on nitrogen-doped reduced graphene oxide (Co-N-rGO), synthesized via a rapid, one-pot microwave-assisted method. Comprehensive characterization by FESEM, TEM, Raman spectroscopy, and X-ray photoelectron spectroscopy confirms the successful formation of atomically dispersed Co(II) centers, coordinated to oxygen-containing functional groups within the graphene matrix, with no evidence of metallic clusters or oxide nanoparticles. The atomically dispersed Co sites act as highly active centers for the oxygen reduction reaction (ORR) in alkaline media, achieving an onset potential of ~ 0.9 V vs. RHE, an average electron transfer number of ~ 3.9 , and a low peroxide yield of $\sim 6\%$, delivering near four-electron transfer efficiency, and outstanding durability that surpasses commercial Pt/C catalysts. First-principles density functional theory (DFT) calculations corroborate the XPS findings and reveal the electronic structure of the Co–O coordination environment, offering atomistic insight into the catalytic mechanism. The synergy between precise site isolation, optimized local coordination, and electronic modulation enables the superior electrocatalytic performance of this Co SAC. This study establishes a versatile and scalable framework for engineering high-performance ORR catalysts featuring non-noble metal single-atom active sites.

In recent years, extensive research has focused on the development of sustainable and efficient energy technologies to address the global demand for cleaner energy sources. Among these, fuel cells have attracted significant attention due to their high energy density and potential to serve as practical alternatives to conventional energy^{1,2}. However, one of the major challenges in fuel cell technology is the sluggish kinetics of the oxygen reduction reaction (ORR) at the cathode, which significantly affects the overall efficiency of the system^{3–6}. To enhance ORR efficiency, electrocatalysts are required to reduce overpotentials and facilitate the four-electron pathway over the two-electron one, leading to the direct formation of water^{7–10}. An electron transfer number near four indicates complete O₂ reduction to H₂O, maximizing efficiency and minimizing harmful peroxide formation. The two-electron pathway produces H₂O₂, which degrades catalysts and fuel cells. Therefore, catalysts favoring the four-electron route are vital for durable, high-performance fuel cells.

Traditionally, noble metals such as platinum (Pt) and palladium (Pd) have been employed as ORR catalysts due to their known high catalytic activity^{11–15}. However, their high cost and limited availability have severely restricted their widespread applications. Recently, affordable alternatives such as zirconium nitride have emerged, demonstrating promising ORR performance in alkaline media¹⁶. Consequently, alternative materials, particularly carbon-based supports decorated with metal species, have emerged as promising ORR electrocatalyst candidates^{7,17–21}. Carbon-based materials exhibit excellent stability, tunable electronic properties, and significantly lower costs compared to noble metals^{22–25}. These properties can be further enhanced by doping with heteroatoms or transition metals. A particularly interesting platform of such a kind is nitrogen-doped reduced graphene oxide (N-rGO), which exhibits ease of further functionalization with transition metals^{26–29}. Moreover, the presence of nitrogen introduces additional active sites and strengthens electronic interactions between the carbon

¹Department of Applied Science and Technology, Politecnico di Torino, Torino, Italy. ²Center for Sustainable Future Technologies@Polito, Istituto Italiano di Tecnologia, Torino, Italy. ✉e-mail: francesca.risplendi@polito.it; micaela.castellino@polito.it

support and metal species, thereby enhancing both catalytic activity and durability^{30–33}.

Similarly, cobalt (Co)-based materials have attracted considerable interest for ORR applications due to their ability to facilitate efficient electron transfer and thus, enhance catalytic performance^{34–37}. In particular, various studies have demonstrated that Co, in the form of metal, oxides, or carbides, can significantly boost ORR activity when incorporated into carbonaceous frameworks such as porous carbons, carbon nanotubes, or graphene-based materials^{38–41}. As a result, several studies have reported on the functionalization of N-rGO with Co in different oxidation states for electrocatalytic applications. A. Ejaz⁴² investigated a cobalt hydroxide [Co(OH)₂] nanoflower-decorated N-rGO system for electrocatalytic sensing, demonstrating the synergistic effects between N doping and Co(OH)₂ in enhancing surface catalytic activity. Similarly, P. Yaengthip et al.⁴³ reported ORR activity in acidic media for a Co-decorated N-rGO material, showing that thermal treatment at 300 °C optimized the catalytic performance by preserving N functionalities. In an alkaline medium, Zhang et al.⁴⁴ observed an ORR peak potential of −0.26 V vs. Ag/AgCl for a cobalt oxide (Co₃O₄)-decorated N-rGO catalyst, demonstrating an electron transfer number close to 4, which is ideal for ORR in the fuel cell applications.

In this work, we present a combined experimental and theoretical investigation aimed at elucidating the structure–activity relationship responsible for the outstanding catalytic performance of Co-functionalized N-rGO (Co-N-rGO). The material is synthesized via a rapid and environmentally sustainable microwave (MW)-assisted hydrothermal process, during which GO undergoes simultaneous reduction, N incorporation, and Co coordination. This one-step synthesis results in the formation of a well-defined tetraphenyl porphyrin (TPP)-like coordination environment, akin to that observed in other metal-containing N-doped systems (e.g., Cu-functionalized rGO)^{25,45,46}. Our findings highlight the distinct role of Co incorporation within this coordination framework in driving the superior

catalytic activity observed. This insight offers a new design principle for the development of efficient single-atom catalysts based on non-noble metals.

Comprehensive characterization of the synthesized Co-N-rGO — performed via field emission scanning electron microscopy (FESEM), transmission electron microscopy (TEM), X-ray photoelectron spectroscopy (XPS), and Raman spectroscopy— confirms the successful adsorption of Co ions on the graphene plane, coordinated by oxygen-containing groups, with no evidence of crystalline structures such as metallic nanoclusters or oxide nanoparticles. The Co is stabilized in a +2-oxidation state and coordinated to oxygen (O)-containing functional groups anchored to the rGO matrix. To identify the atomistic structure of the active site and gain deeper insight into its electronic properties and exceptional electrocatalytic performance, density functional theory (DFT) calculations were performed. These simulations not only support the experimental XPS findings but also elucidate the fundamental role of cobalt in the catalysis of the oxygen reduction reaction. Electrochemical and analytical measurements further confirm the high ORR activity and long-term stability of Co-N-rGO in alkaline media. The integration of advanced characterization techniques with theoretical modeling provides a thorough understanding of the underlying structure–activity relationship, offering valuable guidance for the rational design of next-generation electrocatalysts.

Results

Physical and chemical characterization

The Co-N-rGO was synthesized using a previously established and reproducible microwave assisted method, as reported in our earlier work (refs. 25,45,46) and described in detail in the Supporting Information. To investigate the morphological and structural properties of the synthesized material, FESEM and TEM were first employed. As shown in Fig. 1a, FESEM imaging reveals multilayered graphene-like flakes with extended lateral size at the micrometer scale, consistent with high-quality 2D graphene derivatives. Notably, no signs of morphological degradation or

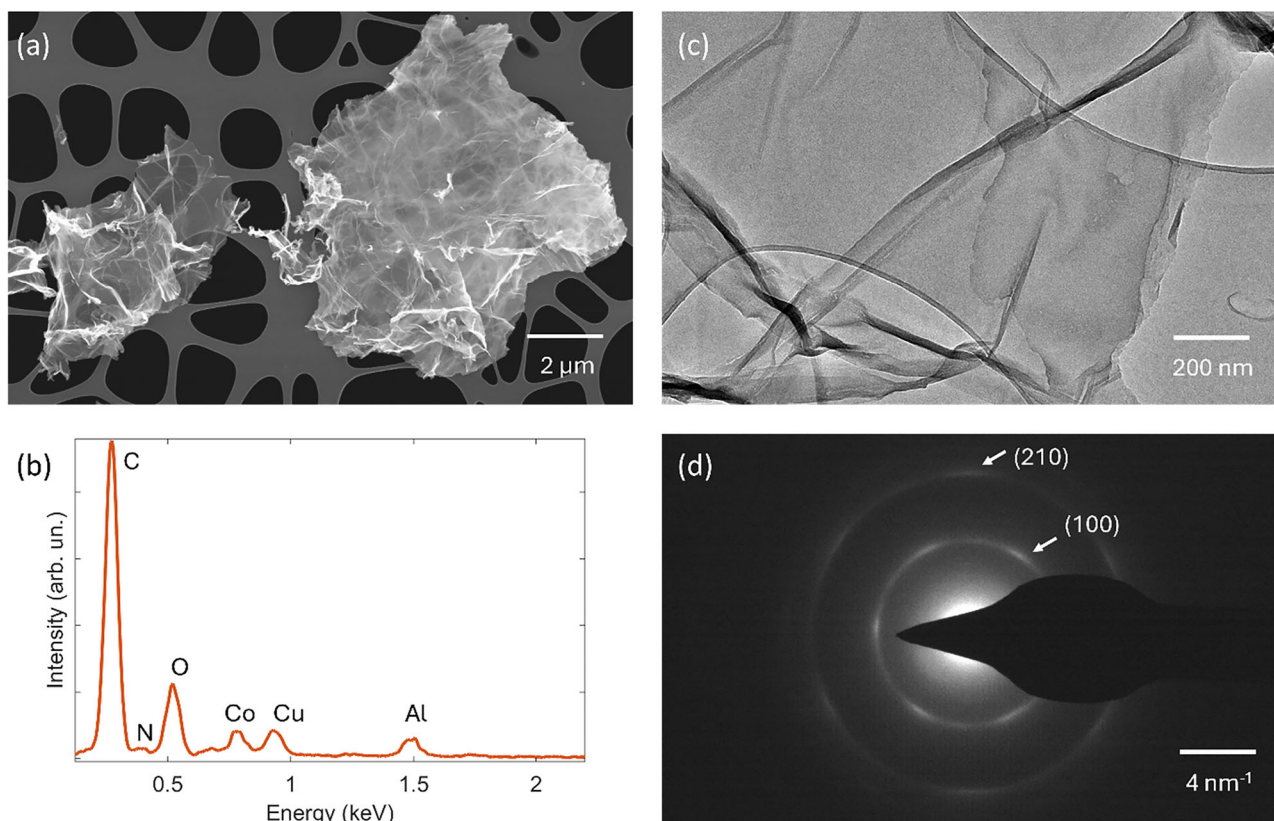


Fig. 1 | Electron microscopy characterization. **a** Representative FESEM image of rGO flakes; **b** corresponding EDX spectrum. **c** Bright Field TEM image of a rGO flake, **d** corresponding electron diffraction pattern typical of multilayered graphene.

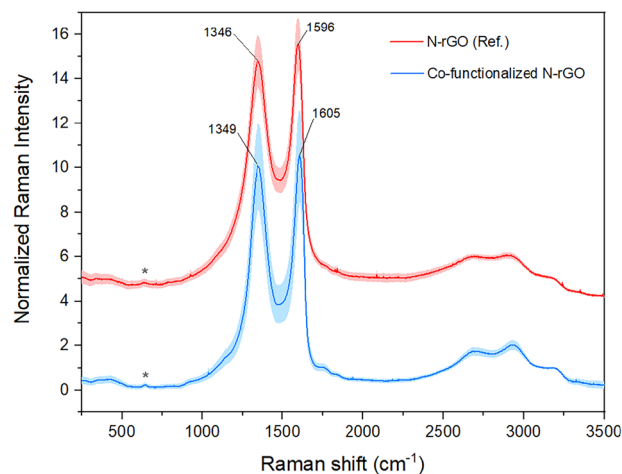


Fig. 2 | Raman spectra of N-rGO and Co-N-rGO. **a** Average Raman spectra of the N-rGO reference (top, red spectrum, $N = 33$) and of the cobalt-functionalized N-rGO nanomaterial (bottom, blue spectrum, $N = 33$). Shaded profiles represent the standard deviation of the mean normalized Raman intensity. The spectra are vertically offset for clarity. A low intensity band at around 640 cm^{-1} (marked with an asterisk) appears in both the cobalt-functionalized N-rGO and the reference N-rGO samples, indicating no univocal relationship with the cobalt-functionalized nanomaterial. This band has been assigned to the density of phonon states in reduced graphene oxide and does not match any characteristic cobalt oxide band.

fragmentation were observed following the microwave-assisted synthesis, confirming the mildness of the process. The presence of cobalt was clearly detected by EDX spectroscopy (Fig. 1b), which reveals distinct peaks for Co, C, and N, along with minor signals from the copper grid (Cu) and the holder (Al).

TEM micrographs (Fig. 1c) further confirm the integrity of the carbonaceous framework at the nanometer scale, showing the absence of crystalline domains that could be attributed to cobalt-based or cobalt oxide phases. Electron diffraction patterns (Fig. 1d) exhibit the typical ring-like features of multilayered graphene with no additional diffraction spots, reinforcing the conclusion that no crystalline phases are present and confirming successful Co inclusion without nanoparticle formation. Nevertheless, Raman spectroscopy provides complementary insights into the structural properties of the catalyst. Spectra of the Co-N-rGO material and a Co-free N-rGO reference (synthesized as in refs. 47, 48) are compared in Fig. 2. In the low-frequency region ($<1000\text{ cm}^{-1}$)⁴⁸, the absence of crystalline cobalt-based fingerprint bands—typically found between 190 and 700 cm^{-1} (Supplementary Fig. 3)—supports the conclusion drawn from TEM imaging, which showed the absence of crystalline domains that could be attributed to cobalt-based or cobalt oxide phases. The only detectable signal in this region is a weak, broad band at $\sim 640\text{ cm}^{-1}$, possibly originating from a high density of vibrational states in defective graphitic domains^{49,50} rather than Co-based species. This interpretation stems from the compelling fact that the same weak band is also present in the reference N-rGO sample (Fig. 2). Moreover, there is a clear absence of match, in terms of both frequency and relative intensity, with the characteristic bands of nanoscale cobalt oxide and hydroxide species, as reported in Supplementary Table 1. Even in the case of CoO(OH) nanoparticles, for which a Raman band at about 641 cm^{-1} is reported⁵¹, a mismatch in terms of relative intensity is apparent; if such a crystalline phase were to be present, a prominent contribution from the most intense mode at 503 cm^{-1} would necessarily also be observed, as a result of its intensity being about 12 times higher than that of the 641 cm^{-1} mode⁵¹. As a result, the Raman spectra do not suggest any presence of crystalline cobalt species within the limit of detection of the technique. Confocal Raman setup excludes any relevant contribution from the glass substrate (Supplementary Fig. 4).

The main spectral features of Co-N-rGO are typical of (N-)rGO, displaying a D band at 1349 cm^{-1} and a G band at 1605 cm^{-1} . The D band arises

from the defect-activated A_{1g} mode (ring breathing), indicative of disordered sp^2 carbon⁵² (e.g., domains with sp^3 -hybridized carbon centers and presence of substitutional nitrogen), while the G band corresponds to the doubly-degenerate E_{2g} mode (sp^2 C–C stretching), which is highly sensitive to disruptions in the planar sp^2 graphitic network^{53,54} and to variations in charge carrier concentration⁵⁵. The second-order Raman features, including the 2D ($\sim 2688\text{ cm}^{-1}$), D + D' ($\sim 2935\text{ cm}^{-1}$), and 2D' ($\sim 3197\text{ cm}^{-1}$) bands, match those of the Co-free N-rGO reference material, suggesting that the fundamental graphitic structure is preserved.

The intensity of the D and G bands (I_D/I_G) ratio (0.95) of Co-N-rGO is nearly identical to that of N-rGO (0.94), indicating a comparable level of reduction and structural disorder in both⁵⁶. However, both D and G bands exhibit significant blueshifts in the Co-containing sample (two-tailed t test, p value $\ll \alpha$, with $\alpha = 0.05$, and a statistical power of 0.9999 for the D band and 1.0000 for the G band, see Supplementary Table 3 and Supplementary Table 4), implying lattice alterations induced by cobalt incorporation. G-band blueshifts are generally attributed to phonon stiffening due to compressive strain or increased doping levels, suggesting that Co atoms or ions may either intercalate or chemically interact with the rGO^{49,57}. While an increase in doping could be directly attributed to cobalt incorporation into the carbon lattice—alongside nitrogen, i.e., co-doping—the presence of compressive strain may stem from a broader and more complex set of factors, such as the intercalation of coordinating ions or surface functionalization by coordinating or electrostatically interacting species^{26,58}.

Moreover, as reported in Supplementary Table 5, a noticeable narrowing of the G band's full width at half maximum (FWHM) is observed in Co-N-rGO (90 cm^{-1}) compared to the reference (114 cm^{-1}), potentially arising from an increased fraction of ordered sp^2 domains⁵⁴ or from high dopant concentrations suppressing phonon–electron decay via Pauli blocking²⁶. Although the specific origin remains ambiguous, these spectral changes reflect significant structural and electronic modifications, highlighting the need for further investigation via XPS.

XPS was employed to probe the chemical states of the elements and get an insight on Co binding configuration. XPS survey spectra (Fig. 3a) confirm the presence of C, N, O, and Co elements. The relative atomic concentrations are consistent with those reported for other metal ion-functionalized N-rGO materials (e.g., Cu-N-rGO in⁴⁵), highlighting the reproducibility and versatility of the synthesis strategy. High-resolution C1s spectra (Fig. 3b) exhibit five distinct components corresponding to sp^2 carbon (284.5 eV), C–O/H/N (285.8 eV), C=O (288.2 eV), COOH (290.2 eV), and the π – π^* shake-up satellite (291.8 eV), mirroring previously reported deconvolutions for related systems^{25,45}.

The N1s region (Fig. 3c) of Co-N-rGO overlaps almost perfectly with that of the cobalt-free reference, suggesting no significant modification in nitrogen speciation or bonding environments. This contrasts with previous findings on Mn-doped samples, where metal coordination with nitrogen atoms was evident from spectral shifts²⁵. Therefore, cobalt interaction with N-rGO does not directly involve nitrogen.

To probe the chemical state of cobalt, high-resolution Co2p spectra were acquired (Fig. 3d). The Co $2p_{3/2}$ peak, accompanied by characteristic satellite features between 782 and 795 eV , is consistent with Co(II) oxidation state⁵⁹. However, fitting using standard models for cobalt oxides failed to reproduce the experimental line shape accurately, likely because these models assume nanoparticulate or crystalline Co oxide phases—absent in our material as verified by TEM. Instead, we adopted a multiplet-splitting-based model from Briggs and Gibson⁶⁰, better suited to describe Co in molecular or coordination environments. The measured $2p_{3/2} - 2p_{1/2}$ separation of 16 eV further confirms Co(II) assignment and suggests a paramagnetic coordination state.

To refine our interpretation, we conducted a targeted literature review on cobalt-containing carbon complexes. The study by Ivanova⁶¹ emerged as particularly relevant, offering a comparative analysis of five structurally distinct Co(II) species. The best agreement with our experimental spectrum was obtained using parameters corresponding to their compound 4, $\text{Co}_9\text{II}(\mu_3\text{-OH})_6(\text{OCCMe}_3)_{12}(\text{OCMe}_2)_2$, where Co^{2+} ions are coordinated

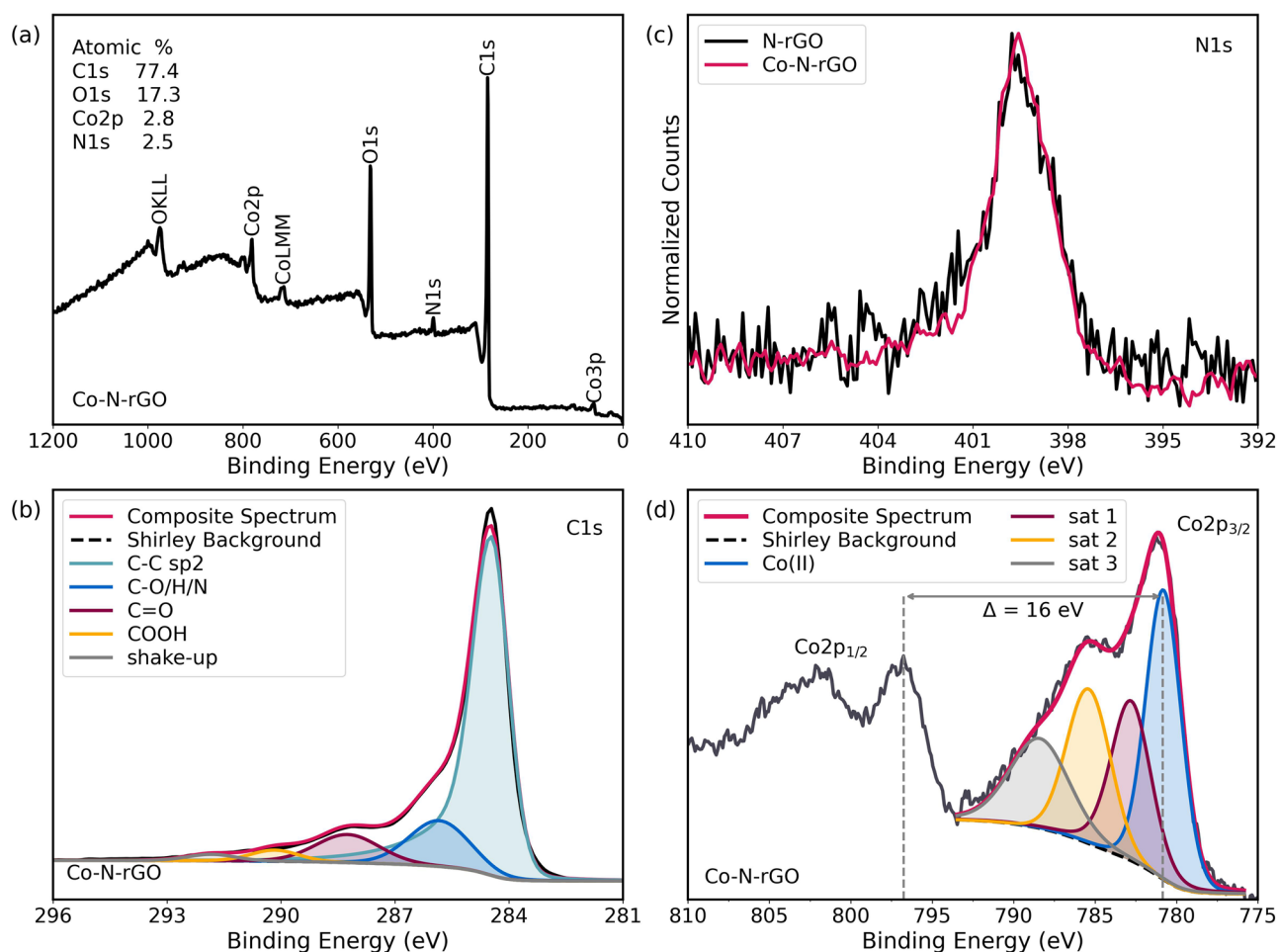


Fig. 3 | XPS analysis of Co-N-rGO: survey and high-resolution spectra of C 1s, N 1s, and Co 2p regions. **a** XPS survey spectrum of Co-N-rGO sample with relative atomic concentration values; **b** XPS HR spectrum for C1s region for Co-N-rGO sample: a fitting procedure has been applied to raw data, which gives as a result five components due to C-C (sp^2), C-O/H/N, C=O, COOH and shake-up satellite due to

$\pi-\pi^*$ transition bonds; **c** XPS HR N1s region for N-rGO and Co-N-rGO samples, showing the almost perfect overlap of the two spectra; **d** XPS HR Co2p region with the Co2p_{3/2} component fitted with four curves due to Co(II) oxidation state and three related satellites as reported in ref. 61. The distance $\Delta=16$ eV is typical for Co(II) paramagnetic arrangement.

by a mixture of carboxylate, carbonyl, and hydroxyl ligands. Further support for this assignment was provided by the satellite-to-main peak intensity ratio, which was 1.85—closely matching the value reported for high-spin Co(II) species in the same study. Complete fitting parameters are listed in Supplementary Table 6.

While these XPS results confirm the oxidation and coordination state of Co, they do not reveal whether cobalt is substitutionally doped into the graphene lattice or merely coordinated at the surface. To gain further insight into the binding nature of cobalt in the Co-N-rGO system, we subjected the Co-N-rGO sample to chemical treatment in H_2SO_4 at room temperature. This procedure, previously employed by Wu et al.⁶² for a nitrogen-cobalt co-doped graphene catalyst, serves to selectively remove Co metallic particles or Co ions bound to the oxygen containing functional groups present at the rGO basal plane without affecting the N-doped framework. Post-treatment XPS analysis (Supplementary Fig. 5a in the Supporting Information) revealed the complete disappearance of the Co2p signal, indicating that all cobalt was removed from the surface. In contrast, the N1s signal (Supplementary Fig. 5b) remained detectable, confirming the stability of nitrogen within the graphene structure, consistent with previous findings²⁵. A slight shift in the N1s peak toward higher binding energy was observed, likely due to protonation of nitrogen atoms by the acidic environment. This behavior confirms that nitrogen is chemically embedded in the structure, while cobalt is only superficially coordinated.

Further confirmation comes from valence band (VB) XPS spectra (Supplementary Fig. 5c), which compare the electronic structure of the as-prepared Co-N-rGO with that of the acid-treated sample and a reference N-rGO. The VB spectrum of the post-treatment sample closely matches that of the reference N-rGO material, while the as-prepared Co-N-rGO shows a distinct increase in spectral intensity near the Fermi level. This enhancement is thus attributed to Co 3d-derived states, which disappear after acid treatment. Taken together, these observations indicate that Co is not embedded within the graphene framework as a substitutional dopant but rather coordinated to functional groups naturally present at sample surface.

DFT-model of Co-rGO

Building on this experimental evidence, we performed DFT calculations to propose structural models for Co^{2+} coordination with the rGO surface. The loss of cobalt after acid treatment (Supplementary Fig. 5c, Supporting Information) and the absence of direct Co-C or Co-N bonding signatures in XPS (Supplementary Fig. 5b, Supporting Information) rule out substitutional doping in the rGO honeycomb structure. Instead, Co^{2+} is coordinated to the rGO basal plane through residual oxygen functionalities, such as epoxide and hydroxide groups, present on the rGO surface, as confirmed by XPS.

Given this evidence, we considered Co-N-rGO structural models in which Co^{2+} forms coordination complexes with ligands consisting of oxygen groups from the rGO basal plane or water molecules and hydroxide ions

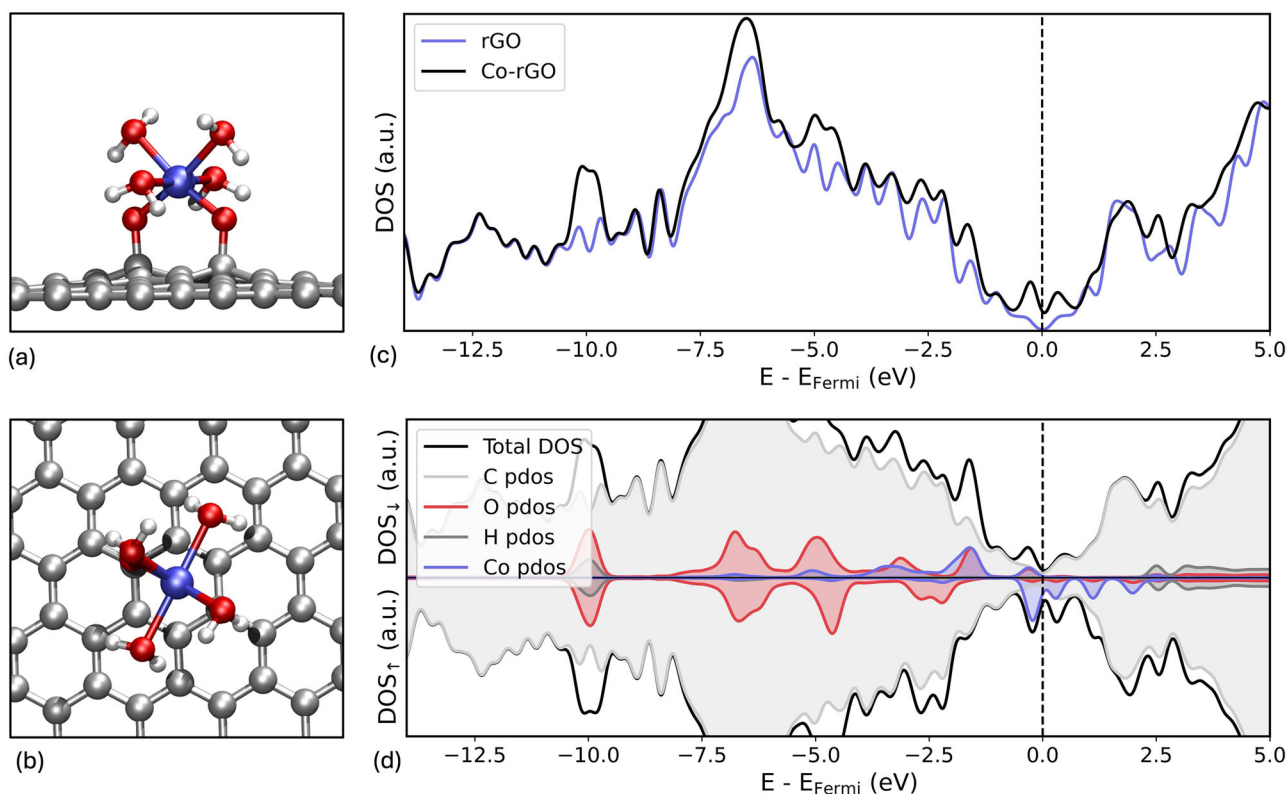


Fig. 4 | Structure and electronic properties of Co-rGO. **a** Top and **b** side views of the modeled structure for Co-functionalized reduced graphene oxide. Gray, red, white, and blue spheres represent carbon, oxygen, hydrogen, and cobalt atoms, respectively. **c** Comparison of the total density of states (DOS) for rGO and Co-rGO.

in the case of Co-rGO, the DOS is averaged over the spin-up and spin-down components. **d** DOS and projected DOS (pDOS) of Co-rGO, with spin-up and spin-down contributions plotted separately.

from the surrounding solution to completing its coordination shell. We modeled several alternative octahedral complexes where the Co^{2+} ion is bound to two vicinal oxygen containing groups of the rGO (Co-OrGO) besides four from OH ions (Co-OH) or water molecules (Co-OH₂) in the electrolyte solution. The geometries of these configurations are shown in Supplementary Fig. 7 of Supporting Information. Our computed Co-O bonding configuration was consistent with earlier findings, which demonstrated that interactions between transition metals and surface oxygen groups lead to stable structures⁴⁵.

In the configuration that best represents our Co-N-rGO catalyst based on XPS data, reported in Fig. 4a, b, the coordination shell of the Co^{2+} anchored to N-rGO is completed by four water molecules, as illustrated in Supplementary Fig. 7a and Supplementary Fig. 7b. Upon structural relaxation, the Co-OrGO bond lengths were found to be 1.91 Å, whereas the Co-OH₂ bond distances ranged from 2.19 Å to 2.25 Å. The resulting complex maintains a +2-oxidation state for cobalt and adopts a high-spin state, closely reproducing the local coordination environment inferred from XPS analysis⁶¹, reinforcing the consistency between experimental observations and computational modeling.

To explore the impact of Co^{2+} coordination on the electronic properties of rGO, we examined the total and projected density of states (DOS and pDOS), shown in Fig. 4c and d respectively. The DOS comparison between pristine rGO (blue curve) and Co^{2+} -decorated rGO (black curve) reveals a significant increase in occupied energy states just below the Fermi level upon introduction of Co^{2+} , consistent with the XPS results presented in Supplementary Fig. 5c of Supporting Information. The pDOS analysis in Fig. 4d demonstrates that the increased energy states are predominantly localized on the Co^{2+} ion and result from the hybridization of Co-3d and O-2p orbitals. The increased density of occupied states near the Fermi level implies greater electronic availability,

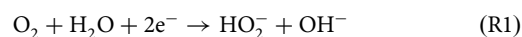
which may facilitate charge transfer processes and thereby enhance the material's catalytic activity.

Electrochemical characterization

Electrocatalytic activity was systematically investigated through a comprehensive set of electrochemical measurements, comparing the Co-functionalized N-rGO with its metal-free counterpart (N-rGO). Experimental details, including cell configuration and electrode preparation, are provided in the Supporting Information. All potentials are referenced to the reversible hydrogen electrode (RHE).

ORR performance was first assessed by cyclic voltammetry (CV) at a scan rate of 10 mV s⁻¹ in O₂-saturated 0.1 M KOH, as shown in Fig. 5a. Co-N-rGO exhibits a distinct cathodic peak centered at ~0.8 V, which vanishes under N₂-saturated conditions, unambiguously confirming its catalytic activity toward ORR. Notably, the onset of reduction for Co-N-rGO is positively shifted by ~200 mV compared to the N-rGO counterpart, highlighting the crucial role of Co in lowering the overpotential. This can be attributed to improved electron transfer and stronger adsorption of ORR intermediates on Co active sites. This enhancement facilitates faster reaction kinetics and lowers the overpotential. These features are consistent with benchmark behavior for high-performance metal-N-C catalysts^{4,63}.

The selectivity and efficiency of the ORR were further elucidated via Rotating Ring Disk Electrode (RRDE) measurements, conducted in O₂-saturated 0.1 M KOH at a scan rate of 5 mV s⁻¹ and a constant rotation speed of 2500 rpm, following established protocols⁶⁴. As shown in Supplementary Fig. 6a, b, the disk current reflects the total ORR activity, encompassing both the 2-electron and 4-electron pathways (R1 and R2)⁶⁵:



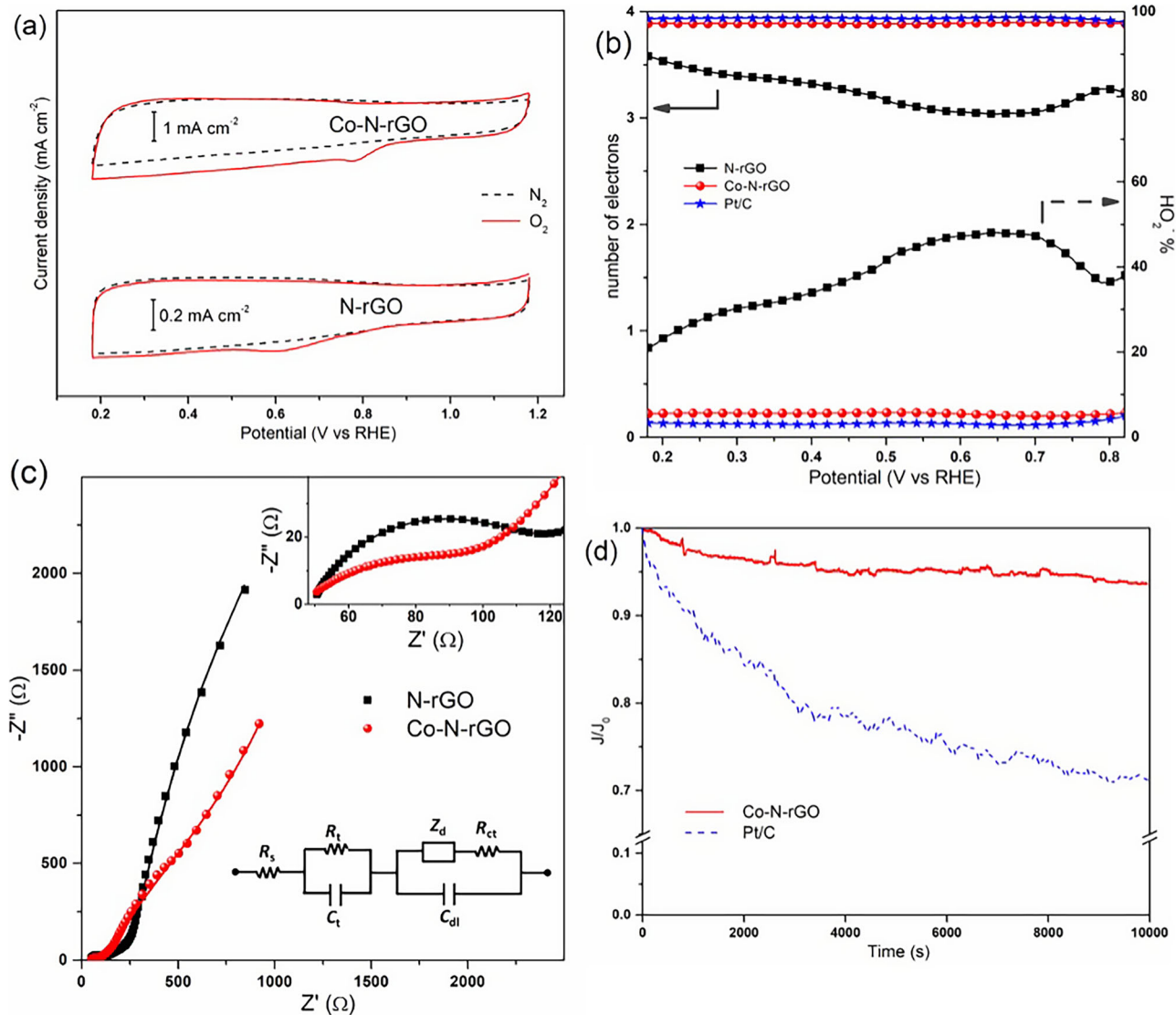


Fig. 5 | Electrochemical evaluation of ORR activity. **a** CV curves recorded in O₂-saturated and N₂-saturated solutions. **b** Comparison of the electron transfer number (left axis) and peroxide percentage (right axis) derived from RRDE measurements.

c Electrochemical impedance spectra: experimental points and fitted curves using the equivalent circuit shown in the inset. **d** CA curves normalized with respect to the initial current density.



Simultaneously, the ring current monitors the oxidation of peroxide intermediates, a parasitic product with well-known corrosive effects⁶⁶.

Both Co-N-rGO and the commercial Pt/C benchmark display ring currents that are two orders of magnitude lower than their corresponding disk currents, pointing to a dominant 4-electron pathway and minimal peroxide formation⁶⁷. In contrast, the N-rGO sample exhibits a ring current only one order of magnitude lower than its disk current, indicating a substantial contribution from the 2-electron route.

Quantitative analysis based on Eqs. (1), (2) enabled calculation of the average number of transferred electrons and the peroxide yield. As summarized in Fig. 5b, Co-N-rGO achieves an electron transfer number close to 4 and a peroxide yield as low as 6%, closely matching the performance of Pt/C. This result underscores the critical role of cobalt in steering the reaction toward the desirable 4-electron reduction, confirming the synergistic interplay between Co and N dopants in modulating the electronic structure and catalytic behavior of the rGO framework.

To gain insight into the catalytic behavior of the Co-N-rGO system, DFT calculations were performed to evaluate the Gibbs free energy ORR profile. Both the 2-electron (partial reduction to HO₂⁻) and 4-electron (complete reduction to OH⁻) pathways in alkaline solution were considered and calculated according to the computational hydrogen electrode (CHE) model^{3,68,69}, as depicted in Fig. 6. The reaction steps modeled along the 4e⁻ pathway were as follows:

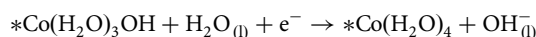
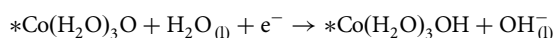
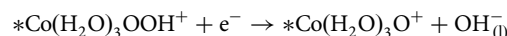
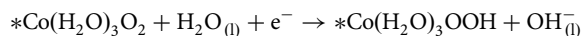
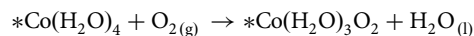
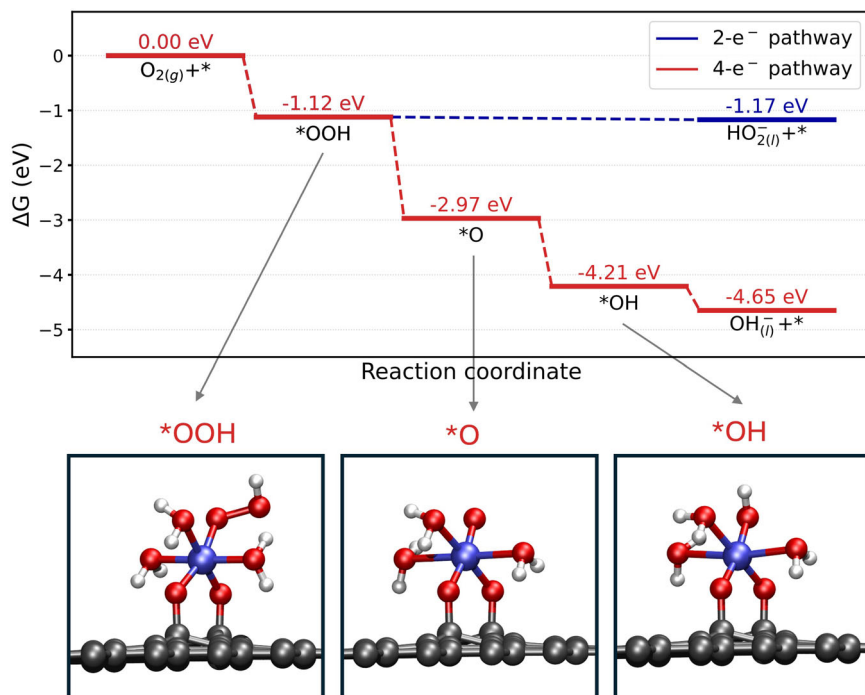
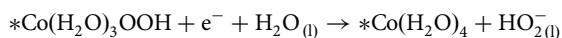
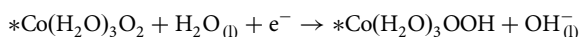
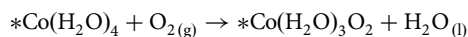


Fig. 6 | Gibbs free energy profile for ORR on the Co-rGO catalyst. The top panel shows the Gibbs free energy diagram for the 2e⁻ (blue curve) and 4e⁻ (red curve) pathways of O₂ reduction, evaluated at 0 V. The bottom panels display the structural configurations of the reaction intermediates along the 4e⁻ ORR pathway. Gray, red, white, and blue spheres represent carbon, oxygen, hydrogen, and cobalt atoms, respectively.



For the 2e⁻ pathway, the modeled steps were:



Where * indicated the rGO substrate anchoring the Co²⁺ ion through two residual surface oxygen atoms (O_{rGO}). The computed free energy diagrams revealed that both ORR pathways are thermodynamically downhill, confirming their spontaneity. However, a marked difference emerged in the limiting potentials: the 4e⁻ pathway exhibited a significantly higher limiting potential (0.44 V) compared to just 0.05 V for the 2e⁻ route. This energetic preference clearly favors the complete 4-electron reduction of oxygen to water on the Co-N-rGO catalyst. These theoretical insights are fully consistent with experimental RRDE data, both converging toward the conclusion that Co functionalization enables highly selective and efficient 4e⁻ ORR catalysis.

To further investigate the origin of the enhanced ORR performance, electrochemical impedance spectroscopy (EIS) measurements were carried out in O₂-saturated 0.1 M KOH at 0.38 V and 2500 rpm (Fig. 5c)⁷⁰. The Nyquist plots exhibit two distinct regions: a high-frequency (HF) semicircle, associated with charge transport within the electrode material, and a low-frequency (LF) arc, reflecting charge transfer processes at the electrode–electrolyte interface and mass transport limitations. The intercept at high frequency provides information on electrolyte and contact resistances⁷¹.

An equivalent circuit model (inset of Fig. 5c) was used to fit the impedance spectra and deconvolute the contributions to the overall resistance. The model includes: (i) a series resistance (R_s) accounting for electrolyte and wiring contributions, (ii) a parallel R_i//C_t element describing bulk transport in the material, and (iii) a parallel combination of a constant phase element with a series of charge transfer resistance (R_{ct}) and diffusion impedance (Z_d), representing interfacial and diffusive processes⁷². To

Table 1 | Resistances obtained from the EIS analysis

Sample	R _s [Ω]	R _i [Ω]	R _{ct} [Ω]	R _d [Ω]
N-rGO	47.7	78.3	35420.0	100.5
Co-N-rGO	46.8	54.2	12732.6	97.1

capture the effects of porosity and surface heterogeneity, constant phase elements with exponents > 0.85 were used instead of ideal capacitors⁷³.

The fitted curves (Fig. 5c) closely match the experimental data, and the extracted parameters are summarized in Table 1. A marked reduction in both R_i and R_{ct} is observed upon Co incorporation, indicating improved electronic conductivity and enhanced charge transfer kinetics. This is consistent with previous findings on Mn- and Cu-functionalized rGO systems^{25,45} and highlights the synergistic role of Co and N-doping in optimizing the electrochemical response of graphene-based electrodes.

The long-term durability of the Co-N-rGO catalyst was assessed via chronoamperometry (CA) at 0.68 V under O₂ saturation and continuous rotation (2500 rpm). As shown in Fig. 5d, the Co-N-rGO sample retained 94% of its initial current after prolonged operation, outperforming the commercial Pt/C benchmark, which exhibited a substantial activity loss. These results confirm the excellent stability of the Co-N-rGO catalyst and underscore its suitability for practical ORR applications, with performance comparable to—or even superior to—that of other state-of-the-art Co-based carbon materials^{38,74–76}.

Discussion

In this study, we have provided a comprehensive characterization of the morphology, structure, and chemical environment of a Co-N-rGO electrocatalyst synthesized via microwave-assisted method. High-resolution FESEM and TEM analyses confirmed the preservation of a multilayered, graphene-like morphology and the absence of cobalt nanoparticles or crystalline cobalt oxide phases, demonstrating the mild and effective nature of the synthesis protocol. Raman spectroscopy revealed slight yet significant modifications to the graphitic framework upon cobalt incorporation, including G-band blueshifts and narrowing, indicative of lattice strain and/or electronic perturbations likely arising from Co coordination at the surface.

XPS analysis provided a detailed picture of the elemental speciation, clearly identifying cobalt in the Co(II) oxidation state. The Co2p spectral lineshape, satellite structure, and valence band features collectively suggest the presence of a high-spin, paramagnetic Co(II) species, distinct from conventional cobalt oxide environments. Importantly, chemical leaching experiments in acidic media eliminated the cobalt signal while leaving the nitrogen signature intact, confirming that cobalt is not incorporated substitutionally into the carbon lattice, but is instead coordinated to surface functional groups.

DFT modeling supported these findings, proposing a stable coordination geometry where Co²⁺ is anchored by oxygen-containing functionalities on the rGO surface and solvated by water molecules. This coordination environment is consistent with the spectroscopic data and the known chemistry of cobalt in aqueous systems. The obtained experimental and computational insight challenge conventional assumptions about substitutional metal doping in carbon-based electrocatalysts, suggesting that surface coordination—rather than bulk incorporation—dominates the local environment of catalytically active metal centers.

The unique coordination environment of Co in the Co-N-rGO catalyst directly translates into an enhanced ORR performance. The catalyst demonstrates a high limiting potential in alkaline media, comparable to those of its Co-free counterpart, alongside excellent current densities and durability over extended operation, comparable to those of commercial Pt/C. Crucially, both experimental data and DFT calculations coherently support a dominant four-electron reduction pathway, confirming the efficiency of the atomically dispersed Co²⁺ active sites. The absence of metallic cobalt nanoparticles and the prevalence of atomically dispersed Co²⁺ species are critical to the observed electrocatalytic activity, underscoring the importance of surface coordination in determining the electrocatalytic behavior.

Our findings not only refine the understanding of Co speciation in N-doped graphene-based systems, but also provide key design principles for the development of future catalysts based on atomically dispersed transition metals. By tuning surface coordination, the catalytic properties can be modulated without compromising the integrity of the carbon-based matrix. Moreover, our study highlights the pivotal role of nitrogen doping, which, despite the absence of direct Co–N coordination, enhances the electronic conductivity of the carbon matrix and facilitates charge transfer during the ORR. This finding underscores the synergistic contribution of N incorporation to the overall catalytic performance of the Co-N-rGO system. These results establish a clear correlation between the local geometry of active sites and their electrocatalytic performance, offering valuable insight for the rational design of efficient and sustainable metal-based single atom electrocatalysts for energy conversion applications.

Methods

Synthesis of the catalysts

All the chemicals were used as purchased without further purification. The bare N doped-rGO, used as reference sample, and Co-N-rGO catalysts were fabricated through the procedure reported by Garino et al.²⁵.

In a typical synthesis, 50 mg of GO powder (Graphenea SA, Spain) was suspended in 30 mL of double distilled water containing 20 mg of urea (Sigma-Aldrich).

In the case of Co-N-rGO catalysts sample, 30 mg of (CH₃COO)₂Co 4H₂O (Sigma-Aldrich) was added and dissolved in the as-prepared suspension. For both samples, the precursor mixtures were sonicated for 40 min and then transferred in a 100 mL Teflon reactor, equipped with pressure and temperature probes, connected with the microwave furnace (Milestone FlexyWave, Milestone Inc., Shelton, Connecticut). The mixtures were irradiated for 15 min at 180 °C (800 W) and then the reactor was cooled to ambient temperature. The final powder samples were obtained by freeze-drying. A portion of the Co-N-rGO sample was then treated at room temperature in H₂SO₄, to test the presence of Co after the acid attack.

Physical and chemical characterizations

Field emission scanning electron microscopy (FESEM, ZEISS Dual Beam Auriga) was used to evaluate the morphology of the studied material. Transmission electron microscopy (TEM, FEI Tecnai F20ST, 200 kV) and energy dispersive X-ray spectroscopy (EDS, EDAX) were used to evaluate the morphology, structure and composition of the studied material. Samples for FESEM and TEM were prepared by suspending the obtained nanocomposite powder in ethanol than dropping the suspension on a TEM Cu grid with carbon film.

A Versaprobe PHI 5000 scanning X-ray photoelectron spectrometer (monochromatic Al K-alpha X-ray source with energy of 1486.6 eV) was used to study the chemical composition of the material. A spot size of 100 μm was used to collect the photoelectronic signal for both high resolution (HR) and survey spectra. Different values of pass energy were exploited: 187.85 eV for survey spectra and 23.5 eV for HR peaks. All samples were analyzed with a combined electron and argon ion neutralization system, to reduce the charging effect during the measurements. Semi-quantitative atomic compositions and deconvolution procedures were obtained using the dedicated Multipak 9.6 software. All core-level peak energies were referenced to the C1s peak at 284.5 eV (sp² C-C/C-H bonds) and the background contribution in the HR scans was subtracted using a Shirley function.

Raman spectroscopy measurements were performed using a WITec alpha300 pyrron confocal microscope, fitted with a lens-based, 600 mm focal length ultra-high throughput spectrometer (UHITS), a Peltier-cooled back-illuminated electron multiplying CCD (EMCCD) camera, a 532 nm excitation line, and a 300 g/mm grating. This configuration affords a spectral resolution that ranges from 2.66 to 2.56 cm⁻¹ in the 1300–1600 cm⁻¹ interval. The Raman spectra of Co-N-rGO and a reference N-rGO sample were obtained by depositing the sample flakes in between a glass microscope slide and a glass cover slip, and focusing on the material with a 100x objective (NA = 0.9). Acquisition parameters were 20 s integration time, 25 accumulations, and a power of 1.2 mW at the objective. To minimize sampling bias, all samples were analyzed as multiple spots (airy disc area ≈ 0.7 μm) randomly selected across different flakes, with N = 33 for both Co-N-rGO and the N-rGO reference. Occasional cosmic rays have been removed via the Repair function on the WITec Project SIX Plus software, which consists in a strict, manual selection of the cosmic ray(s) wavenumbers, as shown in Supplementary Fig. 1 (Supporting Information) All spectra were subjected to a minimalistic baseline correction (WITec Project SIX Plus, vertical translation function) and normalized by the intensity of the 2D' band at ~3190 cm⁻¹. For transparency, all raw spectra utilized for this study are reported in Supplementary Fig. 2 (Supporting Information) and the XY data are available upon request. The statistical significance of band shifts and other spectral parameters reported in the manuscript were assessed via a two-tailed t-test after prior evaluation of the homoskedasticity by the Brown and Forsythe test⁷⁷, while the statistical power was calculated post hoc, using GPower 3.1^{78,79}.

Computational details

All the spin-polarized calculations were performed with Vienna Ab initio Simulation Package (VASP) code^{80–82}. Electronic wavefunctions were expanded in plane-waves (PWs) and exchange correlations were modeled by Perdew Burke Ernzerhof (PBE) functional⁸³. The electron-ion interaction was described using Projected Augmented Wave (PAW) potential^{84,85}. Dispersion interactions were included using the DFT-D2 method⁸⁶. A PW energy cutoff of 400 eV was adopted for all calculations. To investigate the cobalt containing rGO samples, 7 × 7 graphene supercells were employed. A vacuum of 20 Å thickness was introduced perpendicular to the 2D layers to avoid spurious interaction between periodic replicas. The Brillouin Zone (BZ) of graphene was sampled employing a (12 × 12 × 1) Monkhorst-Pack mesh⁸⁷ and reduced accordingly in case of supercells, to maintain consistent k-points density. Structural relaxations were performed by minimizing the atomic forces and convergence was assumed when the maximum component of the residual forces on the ions was lower than 0.01 eV/Å and the total

energies were converged to less than 10^{-4} eV. The optimized graphene lattice parameter was calculated as 2.46 Å, in agreement with the previously reported value⁴⁵.

In addition, to further validate the adopted computational approach, we performed benchmark calculations with the hybrid functional HSE06. The results confirmed the qualitative consistency with PBE + D2, supporting the robustness of our conclusions.

The thermodynamic analysis of electrochemical reaction was conducted within the Computational Hydrogen Electrode (CHE) framework proposed by Nørskov et al.^{68,69,88}, which relates the chemical potential of a proton-electron pair to hydrogen gas via thermodynamic equilibrium at the Reversible Hydrogen Electrode (RHE)⁸⁹. Within this formalism, the reaction free energies are referenced to $\frac{1}{2} G(\text{H}_2) - eU_{\text{RHE}}$ and are identical in acidic and alkaline conditions when expressed on the RHE scale. For example, a hydrogenation step can be represented in acidic media as $* + \text{H}^+ + e^- \rightarrow * \text{H}$ or equivalently in alkaline media as $* + \text{H}_2\text{O} + e^- \rightarrow * \text{H} + \text{OH}^-$, leading to the same free energy change using the relation $\mu(\text{OH}^-) = \mu(\text{H}_2\text{O}) - \mu(\text{H}^+)$. The Gibbs free energy of reaction intermediates X (with X = *OOH, *OH, and *O) was computed as:

$$G_X = E_X + E_X^{\text{ZP}} + \int C_p dT - TS_X + E_{\text{solv}}$$

For the hydroxide and hydroperoxide species, free energies were obtained by referencing to H_2O and $\frac{1}{2} \text{O}_2$ following standard CHE conventions, e.g., $G(\text{OH}^-) = G(\text{H}_2\text{O}) - \frac{1}{2} G(\text{H}_2) - eU_{\text{RHE}}$, while $G(\text{HO}_2^-)$ was constructed from balanced reactions involving O_2 , H_2O , and H_2 , ensuring thermodynamic consistency.

The term E_{solv} accounts for the interaction of the aqueous solvent with the adsorbates, since we assume that all reactions take place in an aqueous environment. The solvation energy E_{solv} was evaluated following the procedure reported in ref. 46.

Where, for the calculation of the enthalpic and entropic corrections, all degrees of freedom were assumed to be vibrational and treated within the harmonic approximation. Chemical potentials for gaseous species (H_2 and O_2) were calculated using standard ideal-gas methods, while those for liquid H_2O and H_2O_2 were obtained from thermochemical data for bulk liquids.

Electrochemical characterization

All the electrochemical characterizations for ORR were performed at room temperature with a CHI760D electrochemical workstation and a ALS RRDE-3A rotating ring disk electrode apparatus. The catalyst samples were deposited onto a glassy carbon disk/Pt ring working electrode (electrode area 0.1256 cm^2) following the procedure reported in ref. 90. A Pt wire was used as the counter electrode and Ag/AgCl (3 M Cl⁻) was used as the reference electrode. All the reported potentials refer to the reversible hydrogen electrode (RHE). Unless otherwise specified, all the measurements were carried out in 3-electrodes configuration (disk/reference/counter electrodes) in O_2 -saturated 0.1 M KOH aqueous electrolytic solution with 2500 RPM rotation speed. A commercial available reference Pt/C catalyst (Sigma-Aldrich) was used to compare the obtained result on the synthesized material.

CV curves were acquired from 0.18 to 1.18 V with a scan rate of 10 mV/s in O_2 - and N_2 - saturated electrolytic solution. RRDE measurements were carried out in 4-electrodes configuration (disk/ring/reference/counter electrodes) by scanning the disk electrode from 0.18 V to 1.18 V (scan rate 5 mV/s) and measuring the currents at disk (I_D) and ring (I_R), while fixing the ring potential at 1.18 V. The number of electrons involved in the reduction reaction (n) and the corresponding percentage of produced peroxide species ($\text{HO}_2^- \%$) were calculated using the equations⁹⁰:

$$n = 4 \times \frac{I_D}{I_D + I_R/N} \quad (1)$$

$$\text{HO}_2^- \% = 200 \times \frac{I_R/N}{I_D + I_R/N} \quad (2)$$

where N is the current collection efficiency of the Pt ring. EIS measurements were performed at fixed 0.38 V potential, with an AC signal of 10 mV amplitude and 10^{-2} - 10^4 Hz frequency range. CA curves were acquired at fixed 0.68 V potential.

Data availability

The data that support the findings of this study are available from the corresponding authors upon reasonable request.

Received: 16 June 2025; Accepted: 1 September 2025;

Published online: 29 September 2025

References

- Liu, Y. et al. A CO_2/H_2 fuel cell: reducing CO_2 while generating electricity. *J. Mater. Chem. A* <https://doi.org/10.1039/d0ta02855j> (2020).
- Huo, W. et al. Digitally-assisted structure design of a large-size proton exchange membrane fuel cell. *Energy Environ. Sci.* <https://doi.org/10.1039/d4ee04713c> (2024).
- Nørskov, J. K. et al. Origin of the overpotential for oxygen reduction at a fuel-cell cathode. *J. Phys. Chem. B* <https://doi.org/10.1021/jp047349j> (2004).
- Wang, J. et al. Quantitative kinetic analysis on oxygen reduction reaction: a perspective. *Nano Mater. Sci.* <https://doi.org/10.1016/j.nanoms.2021.03.006> (2021).
- Chen, M. et al. Atomically dispersed metal catalysts for oxygen reduction. *ACS Energy Lett.* <https://doi.org/10.1021/acsenerylett.9b00804> (2019).
- Katsounaros, I. et al. Oxygen electrochemistry as a cornerstone for sustainable energy conversion. *Angew. Chem. Int. Ed.* <https://doi.org/10.1002/anie.201306588> (2014).
- Yang, L. et al. Carbon-based metal-free ORR electrocatalysts for fuel cells: past, present, and future. *Adv. Mater.* <https://doi.org/10.1002/adma.201804799> (2019).
- Luo, C. et al. The influence of multiple factors on the PtCo_3 catalyst characteristics during the ORR process in proton exchange membrane fuel cells. *Renew. Energy* <https://doi.org/10.1016/j.renene.2024.122263> (2025).
- Li, Y. et al. Revisiting Mo-doped $\text{SrFeO}_{3-\delta}$ perovskite: The origination of cathodic activity and longevity for intermediate-temperature solid oxide fuel cells. *Adv. Funct. Mater.* <https://doi.org/10.1002/adfm.202411025> (2024).
- Song, Z. et al. Regulating coordination environment of atomic dimer catalysts for high performance oxygen reduction reaction in fuel cells. *Appl. Catal. B* <https://doi.org/10.1016/j.apcatb.2024.124970> (2025).
- Zhao, K. et al. Coupled cation-electron transfer at the Pt(111)/perfluoro-sulfonic acid ionomer interface and its impact on the oxygen reduction reaction kinetics. *Nat. Catal.* <https://doi.org/10.1038/s41929-024-01279-1> (2025).
- Rampf, A. et al. A comparative study of the oxygen reduction reaction on Pt and Ag in alkaline media. *ChemElectroChem* <https://doi.org/10.1002/celec.202400563> (2025).
- Zhang, L. Y. et al. Weakening Pd-O bonds by an amorphous Pd layer to promote electrocatalysis. *Small* <https://doi.org/10.1002/sml.202409404> (2025).
- Zhou, M. et al. Nanoscale design of Pd-based electrocatalysts for oxygen reduction reaction enhancement in alkaline media. *Small Struct.* <https://doi.org/10.1002/sstr.202100188> (2022).
- Lyu, Z. et al. Biphasic Pd nanosheets with atomic-hybrid RhOx/Pd amorphous skins disentangle the activity-stability trade-off in oxygen reduction reaction. *Adv. Mater.* <https://doi.org/10.1002/adma.202314252> (2024).

16. Liu, H. et al. Origin of the superior oxygen reduction activity of zirconium nitride in alkaline media. *Chem. Sci.* **14**, 9000–9009 (2023).
17. Hu, C. & Dai, L. Kohlenstoffbasierte metallfreie Katalysatoren für die Elektrokatalyse jenseits der ORR. *Angew. Chem.* <https://doi.org/10.1002/ange.201509982> (2016).
18. Liu, X. & Dai, L. Carbon-based metal-free catalysts. *Nat. Rev. Mater.* <https://doi.org/10.1038/natrevmats.2016.64> (2016).
19. Thompson, S. T. & Papageorgopoulos, D. Platinum group metal-free catalysts boost cost competitiveness of fuel cell vehicles. *Nat. Catal.* <https://doi.org/10.1038/s41929-019-0291-x> (2019).
20. Zhou, X. et al. A review of graphene-based nanostructural materials for both catalyst supports and metal-free catalysts in PEM fuel cell oxygen reduction reactions. *Adv. Energy Mater.* <https://doi.org/10.1002/aenm.201301523> (2014).
21. Choi, S. et al. Reduced graphene oxide-based materials for electrochemical energy conversion reactions. *Carbon Energy* <https://doi.org/10.1002/cey2.13> (2019).
22. He, Y. et al. Metal-nitrogen-carbon catalysts for oxygen reduction in PEM fuel cells: self-template synthesis approach to enhancing catalytic activity and stability. *Electrochem. Energy Rev.* <https://doi.org/10.1007/s41918-019-00031-9> (2019).
23. Wu, G. Current challenge and perspective of PGM-free cathode catalysts for PEM fuel cells. *Front. Energy* <https://doi.org/10.1007/s11708-017-0477-3> (2017).
24. Thompson, S. T. et al. ElectroCat: DOE's approach to PGM-free catalyst and electrode R&D. *Solid State Ion.* <https://doi.org/10.1016/j.ssi.2018.01.030> (2018).
25. Garino, N. et al. Proving the existence of Mn porphyrin-like complexes hosted in reduced graphene oxide with outstanding performance as oxygen reduction reaction catalysts. *2D Mater.* <https://doi.org/10.1088/2053-1583/ab2449> (2019).
26. Bruna, M. et al. Doping dependence of the Raman spectrum of defected graphene. *ACS Nano* <https://doi.org/10.1021/nn502676g> (2014).
27. Pumera, M. Materials electrochemists' never-ending quest for efficient electrocatalysts: the devil is in the impurities. *ACS Catal.* <https://doi.org/10.1021/acscatal.0c02020> (2020).
28. Wang, L. et al. Metal-free[†] catalytic oxygen reduction reaction on heteroatom-doped graphene is caused by trace metal impurities. *Angew. Chem. Int. Ed.* <https://doi.org/10.1002/anie.201309171> (2013).
29. Parvez, K. et al. Nitrogen-doped graphene and its iron-based composite as efficient electrocatalysts for oxygen reduction reaction. *ACS Nano* <https://doi.org/10.1021/nn302674k> (2012).
30. Zhang, W. et al. Role of vacancy defects and nitrogen dopants for the reduction of oxygen on graphene. *ACS Catal.* <https://doi.org/10.1021/acscatal.4c01713> (2024).
31. Wang, Y. et al. Optimizing heteroatom doping for efficient hydrogen peroxide production via oxygen reduction. *ACS Sustain. Chem. Eng.* <https://doi.org/10.1021/acssuschemeng.4c00036> (2024).
32. Bai, P. & Xu, L. Toward a unified pH-performance picture of active sites in nitrogen-doped carbon materials. *Appl. Catal. B* <https://doi.org/10.1016/j.apcatb.2024.124908> (2025).
33. Mazánek, V. et al. Ultrapure graphene is a poor electrocatalyst: definitive proof of the key role of metallic impurities in graphene-based electrocatalysis. *ACS Nano* <https://doi.org/10.1021/acsnano.8b07534> (2019).
34. Tang, C. et al. Asymmetric low-coordination tailoring of single-atom cobalt catalysts enabling efficient oxygen reduction reaction. *Nano Energy* <https://doi.org/10.1016/j.nanoen.2025.110776> (2025).
35. Nasim, F. & Nadeem, M. A. Understanding the mechanism and synergistic interaction of cobalt-based electrocatalysts containing nitrogen-doped carbon for 4 e⁻ ORR. *J. Mater. Chem. A* <https://doi.org/10.1039/d3ta00576c> (2023).
36. Meng, N. et al. Boosting the ORR/OER activity of cobalt-based nano-catalysts by Co 3d orbital regulation. *Small* <https://doi.org/10.1002/smll.202400855> (2024).
37. Gupta, S. et al. A review of cobalt-based catalysts for sustainable energy and environmental applications. *Appl. Catal. A* <https://doi.org/10.1016/j.apcata.2023.119254> (2023).
38. Sun, T. et al. Cobalt-nitrogen-doped ordered macro-/mesoporous carbon for highly efficient oxygen reduction reaction. *Appl. Catal. B* <https://doi.org/10.1016/j.apcatb.2016.04.006> (2016).
39. Li, X. et al. MOF derived Co₃O₄ nanoparticles embedded in N-doped mesoporous carbon layer/MWCNT hybrids: extraordinary bi-functional electrocatalysts for OER and ORR. *J. Mater. Chem. A* <https://doi.org/10.1039/c5ta03900b> (2015).
40. Liu, J. et al. Metallic cobalt nanoparticles embedded in sulfur and nitrogen co-doped rambutan-like nanocarbons for the oxygen reduction reaction under both acidic and alkaline conditions. *J. Mater. Chem. A* <https://doi.org/10.1039/c9ta01234f> (2019).
41. Ma, X. et al. The surface engineering of cobalt carbide spheres through N, B co-doping achieved by room-temperature: in situ anchoring effects for active and durable multifunctional electrocatalysts. *J. Mater. Chem. A* <https://doi.org/10.1039/c9ta03762d> (2019).
42. Ejaz, A. & Jeon, S. Synthesis and application of electrochemically reduced N-RGO-Co(OH)₂ nanocomposite for concurrent detection of biomolecules. *Electrochim. Acta* <https://doi.org/10.1016/j.electacta.2017.03.036> (2017).
43. Yaengthip, P. et al. The ORR activity of nitrogen doped-reduced graphene oxide below decomposition temperature cooperated with cobalt prepared by strong electrostatic adsorption technique. *J. Electroanal. Chem.* <https://doi.org/10.1016/j.jelechem.2022.116366> (2022).
44. Zhang, T. et al. Co₃O₄ nanoparticles anchored on nitrogen-doped reduced graphene oxide as a multifunctional catalyst for H₂O₂ reduction, oxygen reduction and evolution reaction. *Sci. Rep.* <https://doi.org/10.1038/srep43638> (2017).
45. Garino, N. et al. Facilely synthesized nitrogen-doped reduced graphene oxide functionalized with copper ions as electrocatalyst for oxygen reduction. *npj 2D Mater. Appl.* <https://doi.org/10.1038/s41699-020-00185-x> (2021).
46. Risplendi, F. et al. Unravelling electrocatalytic properties of metal porphyrin-like complexes hosted in graphene matrices. *2D Mater.* <https://doi.org/10.1088/2053-1583/ab6a5f> (2020).
47. Garino, N. et al. Microwave-assisted synthesis of reduced graphene oxide/SnO₂ nanocomposite for oxygen reduction reaction in microbial fuel cells. *ACS Appl. Mater. Interfaces* <https://doi.org/10.1021/acsami.5b11198> (2016).
48. Castellino, M. et al. The effect of sulfur and nitrogen doping on the oxygen reduction performance of graphene/iron oxide electrocatalysts prepared by using microwave-assisted synthesis. *Nanomaterials* <https://doi.org/10.3390/nano14070560> (2024).
49. Zafar, Z. et al. Evolution of Raman spectra in nitrogen doped graphene. *Carbon* <https://doi.org/10.1016/j.carbon.2013.04.065> (2013).
50. Dresselhaus, M.S., Dresselhaus, G. Light scattering in graphite intercalation compounds. In: *Light Scattering in Solids III. Topics in Applied Physics*, vol 51 (eds Cardona, M. & Güntherodt, G.) Springer, Berlin, Heidelberg. https://doi.org/10.1007/3540115137_2 (1982).
51. Yang, J. et al. Synthesis and Characterization of Cobalt Hydroxide, Cobalt Oxyhydroxide, and Cobalt Oxide Nanodiscs. *Chem. Soc. Rev.* <https://doi.org/10.1021/jp908548f> (2009).
52. Wu, J.-B. et al. Raman spectroscopy of graphene-based materials and its applications in related devices. *Chem. Soc. Rev.* <https://doi.org/10.1039/C6CS00915H> (2018).
53. Tuinstra, F. & Koenig, J. L. Raman spectrum of graphite. *J. Chem. Phys.* <https://doi.org/10.1063/1.1674108> (1970).

54. Ferrari, A. C. & Basko, D. M. Raman spectroscopy as a versatile tool for studying the properties of graphene. *Nat. Nanotechnol.* <https://doi.org/10.1038/nnano.2013.46> (2013).
55. Lee, H. et al. A review of doping modulation in graphene. *Synth. Met.* <https://doi.org/10.1016/j.synthmet.2018.07.001> (2018).
56. Yap, P. L. et al. Tuning the multifunctional surface chemistry of reduced graphene oxide via combined elemental doping and chemical modifications. *ACS Omega* <https://doi.org/10.1021/acsomega.9b02642> (2019).
57. Akhtar, A. J. et al. Unusual dielectric response in cobalt doped reduced graphene oxide. *Appl. Phys. Lett.* <https://doi.org/10.1063/1.4845536> (2013).
58. Casiraghi, C. et al. Raman fingerprint of charged impurities in graphene. *Appl. Phys. Lett.* <https://doi.org/10.1063/1.2818692> (2007).
59. Biesinger, M. C. et al. Resolving surface chemical states in XPS analysis of first row transition metals, oxides and hydroxides: Cr, Mn, Fe, Co and Ni. *Appl. Surf. Sci.* <https://doi.org/10.1016/j.apsusc.2010.10.051> (2011).
60. Briggs, D. & Gibson, V. A. Direct observation of multiplet splitting in 2p photoelectron peaks of cobalt complexes. [https://doi.org/10.1016/0009-2614\(74\)85350-9](https://doi.org/10.1016/0009-2614(74)85350-9) (1974).
61. Ivanova, T. et al. X-ray photoelectron spectra and electron structure of polynuclear cobalt complexes. *J. Electron Spectrosc. Relat. Phenom.* <https://doi.org/10.1016/j.elspec.2006.12.005> (2007).
62. Wu, H. et al. A graphene-based electrocatalyst co-doped with nitrogen and cobalt for oxygen reduction reaction. *Int. J. Hydrog. Energy* <https://doi.org/10.1016/j.ijhydene.2016.09.074> (2016).
63. Gianola, G. et al. Effect of silica leaching treatment during template-assisted synthesis on the performance of FeNC catalysts for oxygen reduction reaction. *Electrochim. Acta* <https://doi.org/10.1016/j.electacta.2025.146085> (2025).
64. Delmondo, L. et al. Nanostructured Mn_xO_y for oxygen reduction reaction (ORR) catalysts. *Appl. Surf. Sci.* <https://doi.org/10.1016/j.apsusc.2016.03.224> (2016).
65. Kim, W. S. et al. Facile synthesis of perovskite LaMnO₃+δ nanoparticles for the oxygen reduction reaction. *J. Catal.* <https://doi.org/10.1016/j.jcat.2016.10.029> (2016).
66. Dumitrescu, I. & Crooks, R. M. Effect of mass transfer on the oxygen reduction reaction catalyzed by platinum dendrimer encapsulated nanoparticles. *PNAS* <https://doi.org/10.1073/pnas.1201370109> (2012).
67. Garino, N. et al. One-pot microwave-assisted synthesis of reduced graphene oxide/iron oxide nanocomposite catalyst for the oxygen reduction reaction. *ChemSelect* <https://doi.org/10.1002/slct.201601037> (2016).
68. Rossmeisl, J. et al. Electrolysis of water on (oxidized) metal surfaces. *Chem. Phys.* <https://doi.org/10.1016/j.chemphys.2005.05.038> (2005).
69. Rossmeisl, J. et al. Electrolysis of water on oxide surfaces. *J. Electroanal. Chem.* <https://doi.org/10.1016/j.jelechem.2006.11.008> (2007).
70. Sacco, A. et al. Anodically-grown TiO₂ nanotubes: effect of the crystallization on the catalytic activity toward the oxygen reduction reaction. *Appl. Surf. Sci.* <https://doi.org/10.1016/j.apsusc.2017.03.224> (2017).
71. Zeng, J. et al. Advanced Cu–Sn foam for selectively converting CO₂ to CO in aqueous solution. *Appl. Catal. B* <https://doi.org/10.1016/j.apcatb.2018.05.056> (2018).
72. Garino, N. et al. Multifunctional flexible membranes based on reduced graphene oxide/tin dioxide nanocomposite and cellulose fibers. *Electrochim. Acta* <https://doi.org/10.1016/j.electacta.2019.02.095> (2019).
73. Hernández, S. et al. New transparent laser-drilled fluorine-doped tin oxide covered quartz electrodes for photo-electrochemical water splitting. *Electrochim. Acta* <https://doi.org/10.1016/j.electacta.2014.01.037> (2014).
74. Zhu, Z. et al. Construction of a cobalt-embedded nitrogen-doped carbon material with the desired porosity derived from the confined growth of MOFs within graphene aerogels as a superior catalyst towards HER and ORR. *J. Mater. Chem. A* <https://doi.org/10.1039/c6ta05196k> (2016).
75. Zhang, X. et al. Probing the electro-catalytic ORR activity of cobalt-incorporated nitrogen-doped CNTs. *J. Catal.* <https://doi.org/10.1016/j.jcat.2016.10.019> (2016).
76. Zhao, H. et al. Synthesis of cobalt and nitrogen co-doped carbon nanotubes and its ORR activity as the catalyst used in hydrogen fuel cells. *Int. J. Hydrog. Energy* <https://doi.org/10.1016/j.ijhydene.2019.03.271> (2019).
77. Brown, M. B. & Forsythe, A. B. Robust Tests for the Equality of Variances. *J. Am. Stat. Assoc.* <https://doi.org/10.2307/2285659> (1974).
78. Faul, F. et al. Statistical power analyses using G*Power 3.1: Tests for correlation and regression analyses. *Behav. Res. Methods* <https://doi.org/10.3758/BRM.41.4.1149> (2009).
79. Faul, F. et al. G*Power 3: A flexible statistical power analysis program for the social, behavioral, and biomedical sciences. *Behav. Res. Methods* <https://doi.org/10.3758/BF03193146> (2007).
80. Kresse, G. & Hafner, J. Ab initio molecular-dynamics simulation of the liquid-metal–amorphous–semiconductor transition in germanium. *Phys. Rev. B* <https://doi.org/10.1103/PhysRevB.49.14251> (1994).
81. Kresse, G. & Furthmüller, J. Efficient iterative schemes for ab initio total-energy calculations using a plane-wave basis set. *Phys. Rev. B* <https://doi.org/10.1103/PhysRevB.54.11169> (1996).
82. Kresse, G. & Furthmüller, J. Efficiency of ab-initio total energy calculations for metals and semiconductors using a plane-wave basis set. *Comput. Mater. Sci.* [https://doi.org/10.1016/0927-0256\(96\)00008-0](https://doi.org/10.1016/0927-0256(96)00008-0) (1996).
83. Perdew, J. P. et al. Generalized gradient approximation made simple. *Phys. Rev. Lett.* <https://doi.org/10.1103/PhysRevLett.77.3865> (1996).
84. Blöchl, P. E. Projector augmented-wave method. *Phys. Rev. B* <https://doi.org/10.1103/PhysRevB.50.17953> (1994).
85. Kresse, G. & Joubert, D. From ultrasoft pseudopotentials to the projector augmented-wave method. *Phys. Rev. B* <https://doi.org/10.1103/PhysRevB.59.1758> (1999).
86. Grimme, S. Semiempirical GGA-type density functional constructed with a long-range dispersion correction. *J. Comput. Chem.* <https://doi.org/10.1002/jcc.20495> (2006).
87. Monkhorst, H. J. & Pack, J. D. Special points for Brillouin-zone integrations. *Phys. Rev. B* <https://doi.org/10.1103/PhysRevB.13.5188> (1976).
88. Nørskov, J. K. et al. Origin of the overpotential for oxygen reduction at a fuel-cell cathode. *J. Phys. Chem. B* <https://doi.org/10.1021/jp047349j> (2004).
89. Jerkiewicz, G. Standard and reversible hydrogen electrodes: Theory, design, operation, and applications. *ACS Catal.* <https://doi.org/10.1021/acscatal.0c02046> (2020).
90. Garino, N. et al. Microwave-assisted synthesis of reduced graphene oxide/SnO₂ nanocomposite for oxygen reduction reaction in microbial fuel cells. *ACS Appl. Mater. Interfaces* <https://doi.org/10.1021/acscami.5b11198> (2016).

Acknowledgements

We acknowledge funding provided under Italy's National Recovery and Resilience Plan (NRRP), Mission 4—Component 2, “From Research to Business,” through Investment 3.1, “Fund for the Creation of an Integrated System of Research and Innovation Infrastructures” (Call No. 3264, 28/12/2021, from the Italian Ministry of Research), funded by the European Union—NextGenerationEU (Project Code: IR0000027, Concession Decree No. 128, 21/06/2022, CUP: B33C22000710006, Project Title: iENTRANCE). We

acknowledge the “Italian Research Center on High Performance Computing, Big Data and Quantum Computing” (ICSC) funded by the European Union – NextGenerationEU and established under the NRRP, as well as high-performance computing resources and support provided by CINECA through the ISCRA initiative and HPC@POLITO. We also acknowledge financial support under the National Recovery and Resilience Plan (NRRP), Mission 4, Component 2, Investment 1.1, Call for tender No. 104 published on 2.2.2022 by the Italian Ministry of University and Research (MUR), funded by the European Union – NextGenerationEU– Project Title: A Combined Experimental and Theoretical Approach for Single-Atom Catalyst Engineering Towards Tuneable Activity and Selectivity in CO₂ electro-reduction (RECYCLE-CO₂)—Grant Assignment Decree No. 2022FM3LXT. Moreover, this study was also developed in the framework of the research activities carried out within the Project “Network 4 Energy Sustainable Transition—NEST”, Spoke 4, Project code PE0000021, funded under the National Recovery and Resilience Plan (NRRP), Mission 4, Component 2, Investment 1.3—Call for tender No. 1561 of 11.10.2022 of Ministero dell’Università e della Ricerca (MUR); funded by the European Union—Next-GenerationEU. The Raman analysis portion of this project has received funding from the European Research Council (ERC) under the European Union’s Horizon 2020 research and innovation programme (grant agreement No 865819).

Author contributions

F.R. contributed to the conceptualization, formal analysis, investigation, methodology development, project administration, software implementation, supervision, validation, visualization, and writing of both the original draft and the revised version of the manuscript. N.G. contributed to the conceptualization, investigation, and methodology, and participated in the writing of the original draft. J.Z. contributed to the investigation and writing of the original draft. A.S. contributed to the formal analysis, investigation, validation, and writing of the original draft. S.M. contributed to the formal analysis, investigation, methodology, software development, validation, and writing of the original draft. C.D. contributed to the formal analysis, investigation, validation, writing of the original draft, and manuscript revision. L.F. contributed to funding acquisition. M.F. contributed to the formal analysis, investigation, validation, writing of the original draft, and revision of the manuscript. A.C. contributed to the investigation. G.C. contributed to funding acquisition, methodology development, supervision, and manuscript revision. M.C. contributed to the

conceptualization, formal analysis, investigation, methodology development, project administration, supervision, validation, visualization, and writing of both the original draft and the revised manuscript. All authors provided resources and reviewed the manuscript. Corresponding authors: F.R. and M.C. are the corresponding authors of this work.

Competing interests

The authors declare no competing interests.

Additional information

Supplementary information The online version contains supplementary material available at <https://doi.org/10.1038/s41699-025-00604-x>.

Correspondence and requests for materials should be addressed to Francesca Risplendi or Micaela Castellino.

Reprints and permissions information is available at <http://www.nature.com/reprints>

Publisher’s note Springer Nature remains neutral with regard to jurisdictional claims in published maps and institutional affiliations.

Open Access This article is licensed under a Creative Commons Attribution-NonCommercial-NoDerivatives 4.0 International License, which permits any non-commercial use, sharing, distribution and reproduction in any medium or format, as long as you give appropriate credit to the original author(s) and the source, provide a link to the Creative Commons licence, and indicate if you modified the licensed material. You do not have permission under this licence to share adapted material derived from this article or parts of it. The images or other third party material in this article are included in the article’s Creative Commons licence, unless indicated otherwise in a credit line to the material. If material is not included in the article’s Creative Commons licence and your intended use is not permitted by statutory regulation or exceeds the permitted use, you will need to obtain permission directly from the copyright holder. To view a copy of this licence, visit <http://creativecommons.org/licenses/by-nc-nd/4.0/>.

© The Author(s) 2025